Advanced Functional Materials

ADVANCED FUNCTIONAL MATERIALS
www.afm-journal.de

RESEARCH ARTICLE OPEN ACCESS

Where Most Frameworks Degrade: Flexible Bimetallic Phosphonate Crystals as pH-Universal Supercapacitor Electrodes

Tim Müller[1] | Jean G. A. Ruthes[2,3] | Biswajit Battacharya[4] | Dorothee Silbernagl[4] | Patrik Tholen[5] | Aysenur Limon[1] | Gülsüm Kinik[6] | Christoph Janiak[1] | Markus Suta[6] | Franziska Emmerling[4] | Volker Presser[2,3,7] | Gündoğ Yücesan[1]

[1]Institute of Inorganic Chemistry, Heinrich Heine University Düsseldorf, Düsseldorf, Germany | [2]INM – Leibniz Institute For New Materials, Saarbrücken, Germany | [3]Department of Materials Science and Engineering, Saarland University, Saarbrücken, Germany | [4]Department of Materials Chemistry, Federal Institute for Materials Research and Testing, Berlin, Germany | [5]Food Chemistry and Toxicology, Berlin Technical University, Berlin, Germany | [6]Inorganic Photoactive Materials, Institute of Inorganic Chemistry, Heinrich Heine University Düsseldorf, Düsseldorf, Germany | [7]saarene - Saarland Center For Energy Materials and Sustainability, Saarbrücken, Germany

Correspondence: Franziska Emmerling (franziska.emmerling@bam.de) | Volker Presser (volker.presser@leibniz-inm.de) | Gündoğ Yücesan (guendog.yuecesan@hhu.de)

Received: 21 January 2026 | **Accepted:** 23 January 2026

Keywords: batteries | bimetallic phosphonates | supercapacitors | sustainable energy storage

ABSTRACT

Herein, we report the charge storage and plastic properties of the redox-active, bimetallic metal phosphonate framework of [Cu(2,2′-bpy)VO($O_3PC_6H_5$)$_2$]. The flexible crystals of [Cu(2,2′-bpy)VO($O_3PC_6H_5$)$_2$] combine high energy storage with mechanical flexibility on the same platform, which is an unusual and significant property that is not observed in traditional rigid layered electrode materials. In contrast to RuO_2, graphene, or MXenes, which prefer concentrated acidic or basic electrolytes to operate effectively as electrodes, [Cu(2,2′-bpy)VO($O_3PC_6H_5$)$_2$] operates between pH values of 4 and 10 while reaching a specific capacitance of about 140 F/g in H_3PO_4 at pH 4 and in NaOH at pH 10 at 1 mV/s. It also demonstrates high chemical and electrochemical stability between pH 2 and 12 and in lithium hexafluorophosphate for extended periods. The use of [Cu(2,2′-bpy)VO($O_3PC_6H_5$)$_2$] as electrodes eliminates the need for harsh chemical environments, generating more sustainable and environmentally friendly energy storage solutions, and [Cu(2,2′-bpy)VO($O_3PC_6H_5$)$_2$] can be synthesized in water at mild temperatures. The combination of chemical stability, mechanical flexibility of [Cu(2,2′-bpy)VO($O_3PC_6H_5$)$_2$], and compatibility with mild electrolytes makes [Cu(2,2′-bpy)VO($O_3PC_6H_5$)$_2$] a more sustainable alternative to conventional metal oxides, MXenes, and carbon-based electrodes in next-generation supercapacitors and battery technologies.

1 | Introduction

The current material landscape in supercapacitor and battery electrodes includes a diverse range of materials such as MXenes, graphene, carbon nanotubes, activated carbon, metal oxides, conductive polymers, and recently, metal-organic frameworks (MOFs) [1–6]. Each of these material types delivers advantages and limitations in the form of variables such as energy density, power density, electrical conductivity, cycle life, and cost [1–6]. Additionally, structural diversity limitations hinder their further development for improved charge holding. For example, MXenes and graphene provide very high electrical conductivity [7–9]. Still, compared to MOFs, metal oxides, or coordination polymers, they offer very limited structural diversity for optimizing their surface

areas to store electrical energy [10–12]. Despite their stability in various electrolytes, the covalent modifications on graphene and activated carbon are known to be difficult, providing limited structural diversity for further optimizations compared to MOFs or metal-organic solids [13]. MXenes or RuO_2 electrodes usually function under extremely acidic and basic aqueous electrolytes such as 3 M H_2SO_4 or 6 M KOH, while their charge storage is diminished in neutral electrolytes [14–17], and they are still very expensive, requiring high-temperature synthesis [13].

A plethora of electrode materials exists, offering diversity in dimensionality, sustainability, performance metrics, and synthesis-related costs. MXenes are an emerging and diverse 2D material family that enables plentiful applications for electrochemical energy storage and beyond [18, 19]. Yet, the MXene precursor, MAX-phases, typically requires high-temperature synthesis at or above 1000°C, and MXene synthesis involves etching, often involving toxic compounds such as hydrofluoric acid, which limits their sustainable synthesis [20–23]. Despite metal oxides providing high pseudocapacitance, the weaker stability of these materials in water, acids, bases, and aqueous electrolytes is problematic for their further optimization for long-term use [24, 25]. Metal oxides also have limited structural diversity compared to MOFs and coordination polymers [26]. Among other electrode materials, MOFs provide the largest structural diversity and well-established synthetic routes to optimize surface area and energy storage properties [26]. Still, MOFs are known to be insulators, with a very limited number of conductive unconventional MOFs in the literature [27, 28].

We have recently reported a new family of MOF semiconductors based on phosphonic acid linkers, which provide high stability in acids, bases, and electrolytes and offer potentially the richest structural diversity compared to conventional MOFs [29–32]. A few examples of phosphonate-MOFs have been reported to be very stable electrode materials for Li-ion batteries [31, 33]. We have recently reported the semiconducting properties of Cu/V/phosphonate systems. They exhibit large structural diversity, attributed to their wide range of coordination modes, protonation states, and metal oxide oligomerization patterns [34–36]. This structural versatility makes metal/phosphonate systems especially attractive for developing multifunctional, flexible conductive materials. Similarly, independent vanadium oxide moieties are also well-known conductors [37]. In this work, we wanted to study our previously reported organic–inorganic hybrid crystals of [Cu(2,2′-bpy)$VO(O_3PC_6H_5)_2$]. The Cu(II)/V(IV)/oxide chain is surrounded by π-stacked polyaromatic groups (2,2'-bipyridines and phenylphosphonic acids). Such structures hypothetically combine the redox properties of metal oxides and graphene on the same platform, plus improved stability through high-affinity metal phosphonate bonds that are generally resistant to hydrolysis in the presence of acids and bases [30, 38].

Hypothetically, semiconducting flexible crystalline materials would be an exciting class of material that combines mechanical adaptability with electronic functionality [39–41]. Embedding electrical conductivity into such crystals could enable new device architectures, particularly in flexible electronics and energy storage. While most existing flexible crystals rely on weak van der Waals interactions or labile coordination bonds with halogens to achieve flexibility, these approaches often compromise structural integrity or functional performance. To the best of our knowledge, semiconducting behaviour has not been reported yet in flexible crystals [40, 41]. However, achieving a combination of flexibility, mechanical stability, and conducting properties is critical for advancing the design of energy storage devices. Also, again to the best of our knowledge, there are no bimetallic/organic hybrid flexible crystals in the literature with Tauc plots within the semiconducting regime. Herein, we report such crystals of [Cu(2,2′-bpy)$VO(O_3PC_6H_5)_2$] separated and exfoliated into long crystalline sheets, which can be flexed to make a complete loop, as can be seen in Videos S1–S4. We previously reported the crystal structure and antiferromagnetic properties of [Cu(2,2′-bpy)$VO(O_3PC_6H_5)_2$] [42]. Due to its unique flexibility and our recent findings about the electrically conductive behavior of Cu/V-phosphonates, we wanted to explore this organic/inorganic hybrid compound that combines aromatic moieties surrounding the redox-active bimetallic phosphonate chains and its application in Li-ion batteries and supercapacitors.

2 | Results

2.1 | Mechanical Flexibility of [Cu(2,2′-bpy)$VO(O_3PC_6H_5)_2$]

We previously reported the crystal structure and antiferromagnetic properties of [Cu(2,2′-bpy)$VO(O_3PC_6H_5)_2$], which was synthesized hydrothermally in water as a single-phase product above 180°C, and the mechanical properties have not yet been studied [42]. It crystallizes in the monoclinic $P2_1/c$ and contains a rod-shaped chain constructed from corner-sharing of vanadium and copper square pyramids and phosphorus tetrahedra along the crystallographic *a*-axis. Crystals of [Cu(2,2′-bpy)$VO(O_3PC_6H_5)_2$] exhibited complete mechanical flexibility, deforming easily when handled with a metal needle and retaining their deformed shape even after the removal of stress (Figure S1 and Video S1). As seen in Figure 1, face indexing from single-crystal X-ray diffractograms confirmed that the side faces correspond to (001)/(00$\bar{1}$) and (010)/(0$\bar{1}$0), whereas the top face was identified as (100)/($\bar{1}$00), providing a precise determination of the bendable facets.

To gain deeper insight into this behavior, the crystals were examined under a microscope by applying mechanical stress using a pair of forceps and a metal needle in a three-point geometry. Crystals separated and exfoliated into long crystalline sheets, exhibiting remarkable reversible flexibility, even forming a complete loop and returning to their original shape upon stress removal when stressed perpendicular to the CP chains, specifically on the crystallographic face (001)/(00$\bar{1}$), as seen in Video S2. Whereas in the case of thicker crystals, they easily surpassed the elastic limit and entered the plastic deformation regime, stressed upon the same crystallographic face. In contrast, when crystals were stressed along the (010)/(0$\bar{1}$0) and (100)/($\bar{1}$00) faces, brittle fracture was observed (Videos S3 and S4 This plastic bending behavior arises from the presence of a slip plane parallel to (00$\bar{1}$) in the crystal structure. When a mechanical force is applied perpendicular to this slip plane, long-range molecular movement occurs, leading to plastic deformation [43, 44]. In thin crystals, however, the applied stress results only in short-range molecular movement, preventing plastic deformation and allowing the

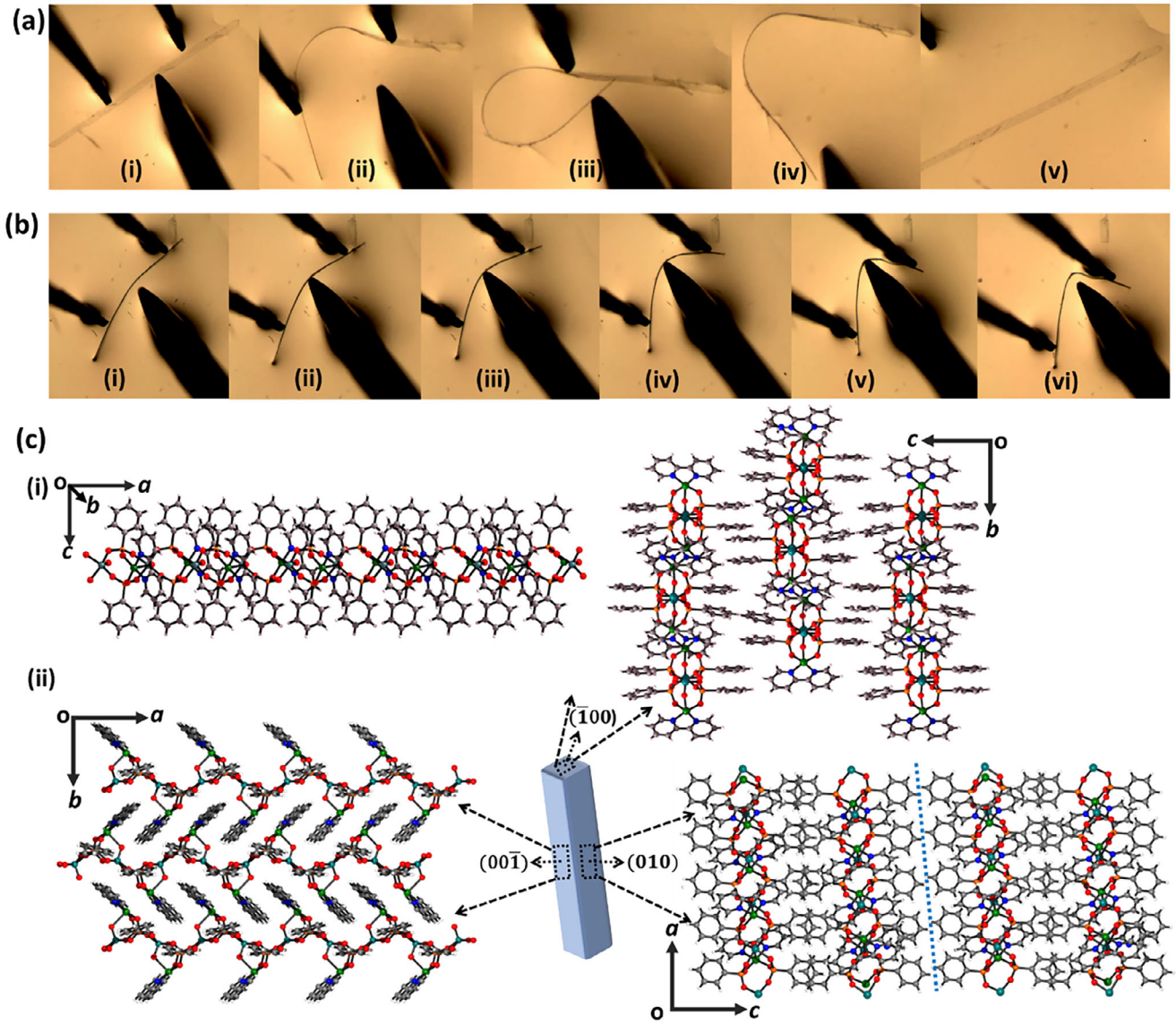

FIGURE 1 | Mechanical properties of $[Cu(2,2'\text{-bpy})VO(O_3PC_6H_5)_2]$ single crystals. (a, b) Optical microscope images of three-point bending experiments performed on single crystals over the (001) crystallographic face: (a) thin and (b) thick crystals. The bending of the thin crystal is fully reversible (a, i–v), whereas the thicker crystal undergoes plastic deformation (b, i–vi). (c) Crystal packing in $[Cu(2,2'\text{-bpy})VO(O_3PC_6H_5)_2]$. (i) Structure of the covalently bonded coordination polymer chain along the crystallographic a-axis. (ii) Crystal packing as viewed along the (100), (010), and (001) faces. Blue dotted lines show a potential slip plane.

crystals to recover their original form once the stress is released. Similar elastic reversible bending and irreversible plastic bending have been recently observed in metal halogen coordination polymers [39, 45]. However, the thickness-dependent flexibility of these systems remains unexplored. In contrast, such behavior is well-documented in molecular organic crystals, but to the best of our knowledge, $[Cu(2,2'\text{-bpy})VO(O_3PC_6H_5)_2]$ is the first metal-organic solid crystal generating such elastic behavior [46] Atomic force microscopy (AFM) force distance curves were used to study the mechanical properties and elastic recovery of crystals with different thicknesses ($t_{bulk} > t_{needle} > t_{sheet}$), as shown in Figure S2. The elastic modulus increased with thickness, with values of 2.75±0.09 GPa for bulk crystals, 2.03±0.05 and 2.20±0.04 GPa for needle-shaped crystals, and 1.79±0.05 GPa for sheet-like crystals (Figure S3 and Table S1). Analysis of the retract curves showed that thinner structures experience less plastic deformation compared to elastic deformation. As a result, the elastic recovery increased significantly as the crystal thickness decreased. This trend agrees well with the qualitative observations from our three-point bending experiments, confirming the superior flexibility and reversible deformation of thinner crystals.

2.2 | Band Gap

Direct and indirect band gaps of the material have been estimated by a Tauc plot generated from the diffuse reflectance spectra (Figure S4) [47, 48]. The compound has an optical band gap in the range between 1.75 and 2.50 eV, which clearly classifies this compound as semiconducting. Despite the low band gap, we were not able to measure electrical conductivity in the single crystals of $[Cu(2,2'\text{-bpy})VO(O_3PC_6H_5)_2]$, which is due to the difficulty

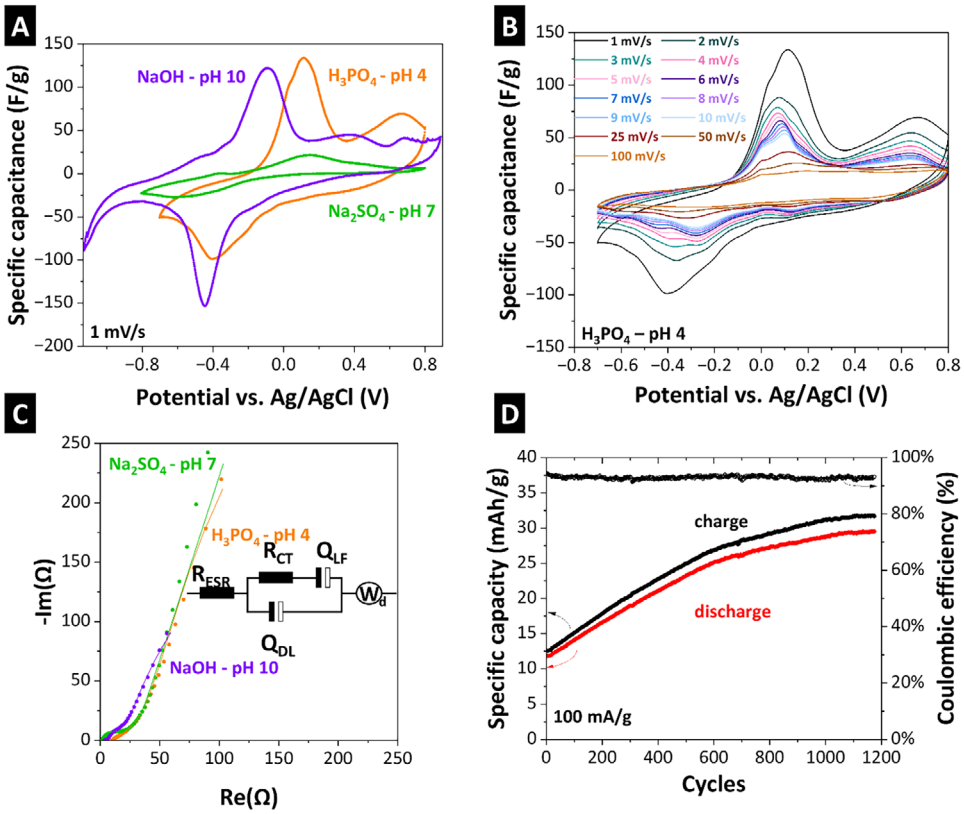

FIGURE 2 | A) Cyclic voltammograms of $[Cu(2,2'\text{-bpy})VO(O_3PC_6H_5)_2]$ at different pH values. B) Cyclic voltammograms of $[Cu(2,2'\text{-bpy})VO(O_3PC_6H_5)_2]$ at different scan rates. C) Electrochemical impedance spectra of $[Cu(2,2'\text{-bpy})VO(O_3PC_6H_5)_2]$ at different pH values. D) Galvanostatic cycling with potential limitation at 100 mA/g for 1200 cycles of $[Cu(2,2'\text{-bpy})VO(O_3PC_6H_5)_2]$ in organic electrolyte $LiPF_6$ 1 M in EC:DMC (1:1 by volume) vs. Li^+/Li as reference and counter-electrode.

of measuring the electric conductivity in isolated rod-shaped structure of $[Cu(2,2'\text{-bpy})VO(O_3PC_6H_5)_2]$, and also due to the twinned crystal structure that can be cracked and exfoliated, which generate limited contact within the crystal.

2.3 | Electrochemical Stability and Energy Storage

The material was tested in different aqueous environments at pH 4, 7, and 10. Cyclic voltammograms shown in Figure 2A corroborate the preliminary observations about the chemical stability of $[Cu(2,2'\text{-bpy})VO(O_3PC_6H_5)_2]$ along with reversible redox peaks, which decay in intensity in different scan rates, shown in Figure 2B. Given the presence of two electroactive metallic centers within the compound, potential shifts observed with increasing scan rates and varying pH suggest a strong correlation between reaction kinetics and ionic interactions in the electrolyte [49]. Moreover, this also suggests that the material is electrochemically active not only in the metallic center, as other structural groups directly impact diffusion kinetics, highlighting the versatility of the synthesized material [50]. Furthermore, there are slight deviations between environments, with a small difference from alkaline to acidic, further reinforcing the chemical stability of the material.

At neutral pH, slower reversible redox kinetics and lower specific capacitance indicate a shift toward diffusion-dominated charge storage over capacitive mechanisms. As seen in Figure 2A,B, the specific capacitance for the electrodes in aqueous H_3PO_4 (pH 4) and aqueous NaOH (pH 10) electrolytes reaches approximately 140 F/g at a low scan rate of 1 mV/s, indicating efficient charge storage due to enhanced ion accessibility and Faradaic contributions under these conditions. MXenes and carbon-based electrodes usually require very concentrated acidic, aqueous 3 M H_2SO_4 and aqueous basic electrolytes 6 M KOH to provide similar capacitance values [15, 51, 52].

Complementary to the preliminary electrochemical analysis, the electrochemical impedance spectra shown in Figure 2C suggest that the system kinetics are directly associated with the electrolyte, as investigated with an equivalent circuit in the inset. At high frequencies, the material shows a partial semi-circle in the Nyquist plot, indicating a Faradaic reaction between electrode and electrolyte, with a charge transfer resistance value of 9.91 Ω at pH 4, 1.64 Ω at pH 7, and 2.53 Ω at pH 10, as observed in the redox peaks. At low frequencies, there is a combination of diffusional and capacitive behavior, with the presence of a second charge transfer resistance, which suggests charge intercalation into the inner electroactive sites of the material. This further supports the observation of reactive chemical groups occluded in the near-surface volume of the material. The fit of the Nyquist plots can be found in Table S2.

To better understand the energy storage process, in addition to using $[Cu(2,2'\text{-bpy})VO(O_3PC_6H_5)_2]$ as the working electrode and activated carbon as the counter electrode, we also prepared

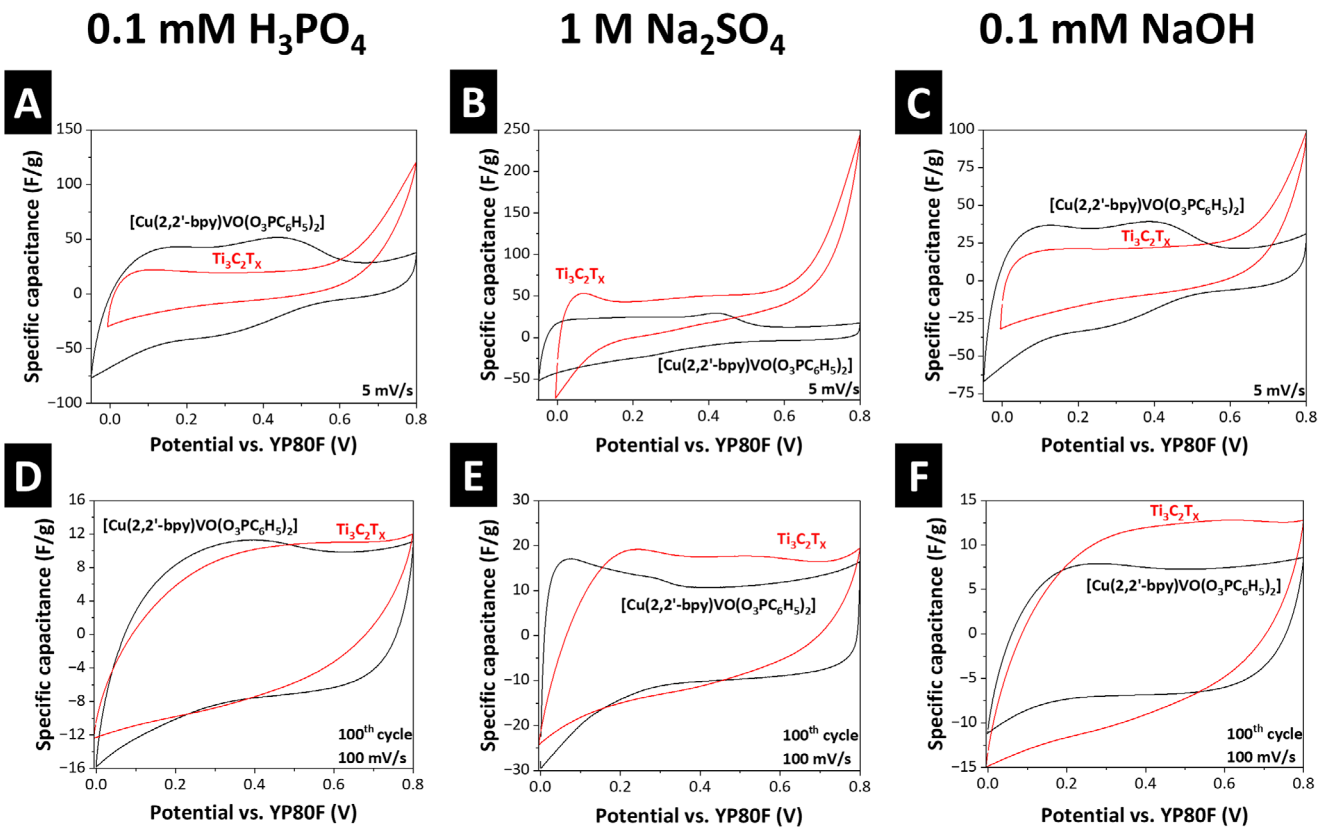

FIGURE 3 | Cyclic voltammograms for comparison of electrochemical behavior between $[Cu(2,2'\text{-bpy})VO(O_3PC_6H_5)_2]$and $Ti_3C_2T_X$ MXene at 5 mV/s in A) pH 4, B) pH 7, and C) pH 10. Comparison at 100 mV/s in D) pH 4, E) pH 7, and F) pH 10.

two-electrode cells with $Ti_3C_2T_X$. As seen in Figure 3A–C, the cyclic voltammograms at 5 mV/s and 100 mV/s display a quasi-rectangular shape in the different electrolytes, highlighting the pseudocapacitive behaviour of $[Cu(2,2'\text{-bpy})VO(O_3PC_6H_5)_2]$, as suggested by the EIS spectra of the electrodes. In comparison with MXene under the same conditions, $[Cu(2,2'\text{-bpy})VO(O_3PC_6H_5)_2]$ shows comparable values of specific capacitance in the used electrolyte conditions at pH 4, 7, and 10. Table S3 summarizes the specific capacitance of the known MOFs in the literature in different electrolyte conditions for comparison. As each of the MOFs reported in the literature was studied in a different electrolyte system, it was not possible to fully compare their capacitance values. $[Cu(2,2'\text{-bpy})VO(O_3PC_6H_5)_2]$ operates in a large pH range compared to the MOFs in the literature, which indicates its advantage, as it can be used under a variety of electrolyte conditions in a dynamic pH range.

The *b*-value analysis in the different electrolyte conditions was performed, indicating a significant diffusional contribution as the scan rate increases, as shown in Figure S5A–C [53, 54]. Using a high specific current of 1 A/g, we conducted extended galvanostatic charge/discharge cycling (Figure S5D–F). Overall, after an initial decrease, the performance was stable at a low amplitude. After 10 000 cycles, the structural integrity of the electrodes was investigated again by Raman spectroscopy, XRD, and SEM-EDX (Figure S6). The diffractograms shown in Figure S6A indicate the characterizing reflectance around 18°2θ, a characteristic signal of the pristine phosphonate $[Cu(2,2'\text{-bpy})VO(O_3PC_6H_5)_2]$ even after cycling in different electrolytes at pH 7 and 10, which is in alignment with Raman spectroscopy (Figure S6B). The electron micrographs shown in Figure S6C–G further support the stability of the $[Cu(2,2'\text{-bpy})VO(O_3PC_6H_5)_2]$ as crystals are visible and intact. Due to the potential formation of extensive EEI at pH 4, it was not possible obtain a reasonable X-ray diffractogram, although some crystals are visible in Figure S6E. The EDX mapping shown in Figures S7 and S8 indicates a homogenous distribution of elemental composition of $[Cu(2,2'\text{-bpy})VO(O_3PC_6H_5)_2]$ in the prepared electrodes.

The electrochemical performance in an organic environment was also investigated in a lithium-ion battery system using a lithium hexafluorophosphate electrolyte (Figure 3D). The electrochemical stability of the material is once again highlighted, with the maintenance of operation after 1000 cycles of GCPL at 100 mA/g and an increase in capacity until a plateau is reached at 32 mAh/g. Although the charge storage of $[Cu(2,2'\text{-bpy})VO(O_3PC_6H_5)_2]$ is limited when operated as a lithium-ion battery, the prolonged chemical stability and the structural versatility of metal phosphonates are significant indicators that they can be used to develop the next-generation long-lasting lithium-ion battery electrodes.

Figure S9A,B shows the cyclic voltammetry in $LiPF_6$ 1 M electrolyte that indicates a quasi-reversible diffusion-controlled mechanism, suggesting an intercalation mechanism, typical of battery-type materials. The sequential peaks suggest two one-electron redox reactions from distinct metallic centers. The first peak at 1.75 V vs. Li^+/Li is associated with the oxidation of $V^{(IV)}$ to $V^{(V)}$, while the peak around 2.5 V vs. Li^+/Li relates to the oxidation of $Cu^{(I)}$ to $Cu^{(II)}$ [55–57]. As for the reduction peaks at 1.5 and 0.5 V vs. Li^+/Li, they correspond to the reduction

of $Cu^{(II)}$ to $Cu^{(I)}$ and $V^{(V)}$ to $V^{(IV)}$, respectively [57]. These redox reactions suggest a two-step process involving Cu and V redox couples with potential hysteresis due to possible structural changes and kinetic limitations during the Li^+ insertion in the [Cu(2,2′-bpy)$VO(O_3PC_6H_5)_2$] framework, suggested by the galvanostatic charge-discharge pattern in 1,200 cycles, shown in Figure S9D [58]. Furthermore, there is no indication of an electrochemical contribution of the 2,2'-bipyridine ligand since it does not undergo redox reactions in this potential window, suggesting that it acts as a structural scaffold [42]. Still, the redox potential displacements may indicate that the electronic delocalization of the ligand impacts the diffusion kinetics.

The theoretical capacity of the [Cu(2,2′-bpy)$VO(O_3PC_6H_5)_2$] is 89 mAh/g, considering a two-electron transfer mechanism between $Cu^{2+} \leftrightarrow Cu^{+}$ and between $V^{5+} \leftrightarrow V^{4+}$. During galvanostatic cycling with potential limitation, although the specific capacity is relatively low, the increase within each cycle is highlighted. This could indicate that the material requires an activation step to allow more electroactive sites to undergo redox reactions, which would be related to the mechanical stress of the Li^+ intercalation of each cycle. To put in perspective, Table S3 compares the specific capacity of our material with other reported MOF/phosphonates.

2.4 | Chemical Stability

Metal oxides are known for their high thermal stability but often exhibit limited chemical stability, especially in the presence of acids, bases, and aqueous electrolytes [59]. While transition metal phosphonates are known to be insoluble in water, a comprehensive study of their solubility constants has not been reported in the literature [38]. However, related copper phosphonates are employed as anticorrosion agents, such as protecting archeological sites from water and acid rain damage [60]. Phosphonates exhibit a very strong metal binding affinity; for example, the structurally analogous phosphonates demonstrate 4.5 orders of magnitude higher metal binding affinity compared to isostructural carboxylate ligands [61]. Furthermore, phosphates form insoluble copper salts with reported solubility product constants around 10^{-37} [62]. This suggests the use of semiconducting phosphonates in electrochemical applications to improve the stability of Li-ion batteries or supercapacitors and limit the hydrolysis in the presence of an aqueous environment. This inherent stability of metal phosphonates is also important when employing a wide range of electrolytes to optimize charge storage potential. Therefore, in this work, we investigated the chemical stability of [Cu(2,2′-bpy)$VO(O_3PC_6H_5)_2$] in acidic (HCl), basic (NaOH), and organic solvents. For this purpose, 15 mg of crystals of [Cu(2,2′-bpy)$VO(O_3PC_6H_5)_2$] were weighed into sample vials and stirred rigorously in 10 mL of the respective medium for one week at room temperature. Subsequently, the samples were re-analyzed using X-ray diffraction (Figure S10A,B) after one week of rigorous stirring. As seen in Figure S10A,B, [Cu(2,2′-bpy)$VO(O_3PC_6H_5)_2$] crystals, after rigorously stirring between pH 2 and 12, retain their characteristic diffraction reflections, indicating high structural integrity within this pH range for one week. No new peaks have been observed within this pH range, suggesting that phase purity is retained after one week.

As can be seen in the scanning electron micrographs (Figure 4), despite vigorous stirring, the crystal edges remain sharp, suggesting there is no or very minimal dissolution between pH 2 and 12 after one week. At pH 1, the crystals were visually present after 3 h, with a slight blue coloring of the acid solution after stirring. After 24 h, the acid solution became blue-colored with a solid precipitate. After one week in 1 M HCl, a very limited presence of phosphorus element can be observed in SEM-EDX, indicating that the majority of the phenylphosphonic acid is protonated and released as a free acid (Figures S11–S25). As seen in Figure 4, at pH 14, some of the original structure is still present after one week of rigorous stirring in 10 mL of 1 M NaOH, indicating strong stability in the basic medium. Overall, the chemical stability tests in various pH values demonstrate that the material exhibits high stability across a broad range of conditions, except for significant degradation observed only at pH 1 after one day.

2.5 | Effect of pH on Crystal Structure and Morphology

As seen in Figures S11–S25, at low pH values, the scanning electron micrographs reveal some exfoliation while retaining the original X-ray diffractogram. At mild pH values of 4, the micrograph shows intact crystals and smooth surfaces. At higher pH values (10 and 12), the bulk structure is maintained, as confirmed by X-ray diffraction. Still, significant exfoliation into thin layers of crystals occurs at higher pH values while retaining the original crystal structure. Especially at pH 12, pronounced exfoliation results in the formation of thin rods peeling off the crystals. As the crystal edges remain sharp, no dissolution of the crystals at pH 12 is observed. These observations indicate that the material can withstand acidic and alkaline conditions without degradation after one week (and continuing) of rigorous stirring of 15 mg of crystals in 10 mL of corresponding acid and base concentrations.

2.6 | Effect of Organic Solvents on Structure and Morphology

As large sections of [Cu(2,2′-bpy)$VO(O_3PC_6H_5)_2$]are composed of aromatic phenyl and bipyridine moieties, we wanted to further test the stability of [Cu(2,2′-bpy)$VO(O_3PC_6H_5)_2$] in the presence of common organic solvents. Scanning electron micrographs (Figure 4) illustrate the exfoliation or peeling of [Cu(2,2′-bpy)$VO(O_3PC_6H_5)_2$] crystals after stirring for 1 week in 10 mL of a variety of organic solvents. The crystals still retain their characteristic diffraction reflections after exfoliation. In polar protic solvents such as methanol, ethanol, and 2-propanol, the crystals maintain their original crystal shape, which is confirmed by the sharp and well-defined X-ray reflections. Aprotic solvents such as DMF (N,N-dimethylformamide), DMAc (dimethylacetamide), and EtOAc (ethyl acetate) help the exfoliation of larger crystals form into a fibrous or fiber-like structure. The X-ray diffractograms indicate that the bulk crystal structure remains intact. Acetic acid (AcOH) also induces a significant exfoliation of the larger crystals, resulting in a fibrous appearance due to the flexibility of the crystals. Overall, [Cu(2,2′-bpy)$VO(O_3PC_6H_5)_2$] material is very robust under extreme chemical environments

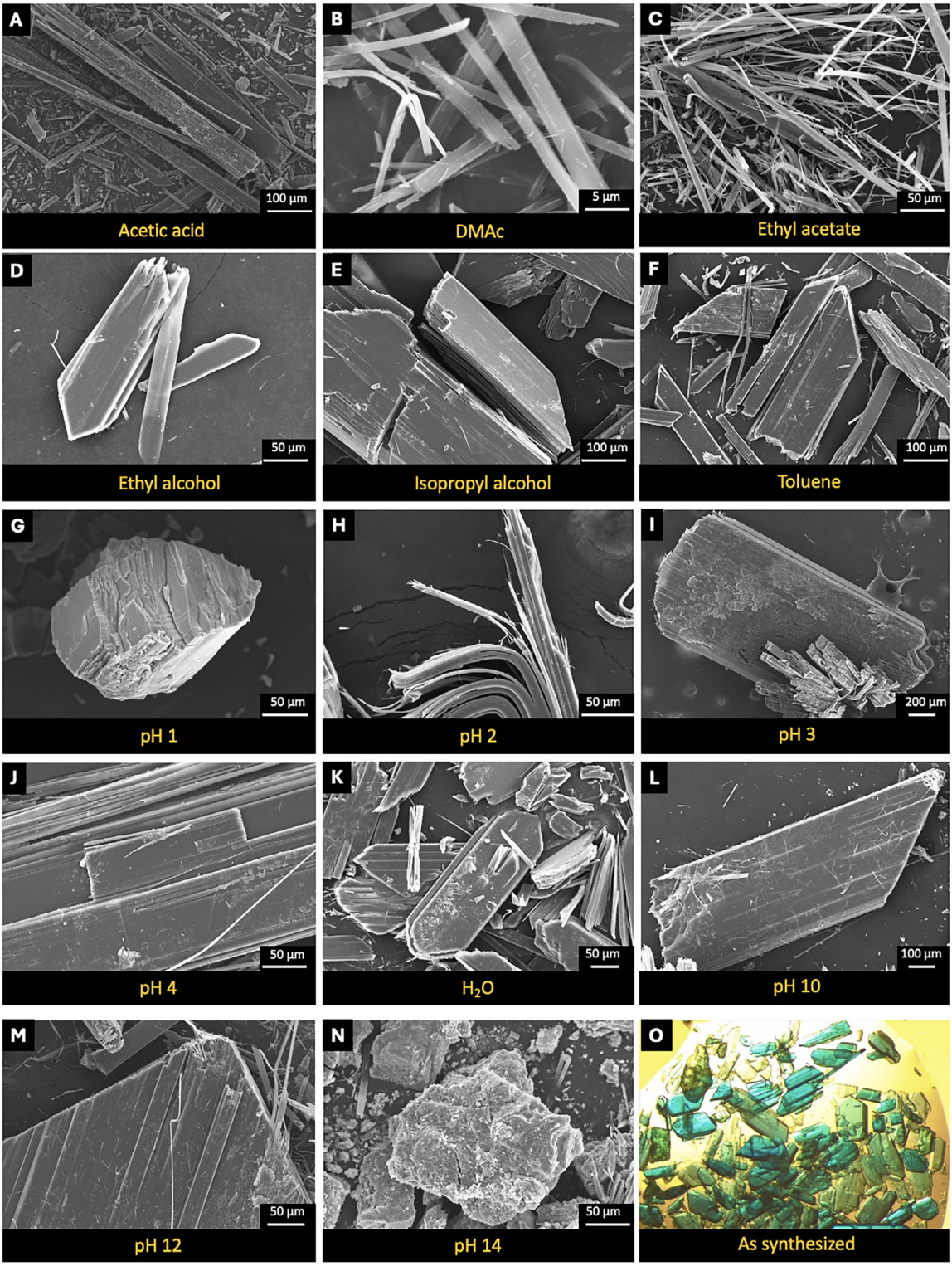

FIGURE 4 | Scanning electron micrographs of [Cu(2,2′-bpy)VO($O_3PC_6H_5$)$_2$] after stirring for 1 week under different pH conditions and in common organic solvents; a) acetic acid b) N,N-dimethylacetamide c) ethylaceatea d) ethyl alcohol e) isopropyl alcohol f) toluene g) pH1 h) pH 2 i) pH 3 j) pH 4 k) in water l) pH 10 m) pH 12 n) pH 14 and o) stereo microscope pictures of the crystals after synthesis.

and retains its structural integrity under a wide range of aqueous and organic conditions. Furthermore, crystals exfoliate at the brittle (010)/(0$\bar{1}$0) and (100)/($\bar{1}$00) faces while no deformation is observed in the flexible face of [Cu(2,2′-bpy)VO($O_3PC_6H_5$)$_2$], generating hair-like exfoliated crystal bundles (Figure 4).

The exfoliation behavior observed at alkaline pH values is particularly interesting, as it increases the surface of [Cu(2,2′-bpy)VO($O_3PC_6H_5$)$_2$] crystals and potentially improves the interaction with electrolytes, leading to better charge storage capacity, which is a critical parameter for supercapacitors and batteries.

The stability of the material, even after exfoliation, is confirmed by consistent X-ray diffractograms (Figure S10), indicating that the core coordination framework remains intact. The observed structural stability in alkaline conditions could help increase the long-term performance and durability of batteries and supercapacitors.

2.7 | Thermal Stability

The thermal stability of [Cu(2,2′-bpy)VO($O_3PC_6H_5$)$_2$] was determined using thermogravimetric analysis (TGA), as shown in Figure S26. The compound exhibits high thermal stability, with only a minor mass loss of approximately 3.5% observed up to 410°C. This is attributed to the evaporation of the surface-adsorbed water vapor. Above 410°C, a significant weight loss occurs, corresponding to the decomposition of the 2,2'-bipyridine and phenylphosphonic acid (PPA) ligands of the coordination polymer. The decomposition associated with 2,2′-bipyridine loss is observed between 410°C and 460°C, although the steps may be overlapping. Subsequently, between 460°C and 610°C, further decomposition associated with the loss of PPA occurs, resulting in a residue of approximately 49.6 mass% at 610°C, which is nearly equivalent to the theoretical 51 mass% corresponding to the inorganic components of [Cu(2,2′-bpy)VO($O_3PC_6H_5$)$_2$]. Beyond 610°C, an additional minor loss of approximately 2 mass% is observed up to 1000°C, likely due to the gradual sublimation of P_4O_{10} or the loss of oxygen from CuO or VO_2. These findings confirm that [Cu(2,2′-bpy)VO($O_3PC_6H_5$)$_2$] exhibits high thermal stability, making it a promising candidate for applications requiring stability under elevated temperatures. The hydrothermal synthesis at 185°C–230°C is also indicative of the intrinsic stability of [Cu(2,2′-bpy)VO($O_3PC_6H_5$)$_2$] in an acidic aqueous environment.

3 | Conclusions

Herein, we report the first flexible bimetallic crystals for energy storage applications in the literature. The mechanically flexing crystals of [Cu(2,2′-bpy)VO($O_3PC_6H_5$)$_2$] have the potential to serve as a supercapacitor material due to their favorable electronic properties and chemical and structural stability. The crystals of [Cu(2,2′-bpy)VO($O_3PC_6H_5$)$_2$] could be exfoliated into thin, flexible sheets without losing the original crystal structure. The flexibility of single crystals can be utilized to manufacture supercapacitors in various shapes and forms. The chemical and thermal stability of [Cu(2,2′-bpy)VO($O_3PC_6H_5$)$_2$] is much better compared to the traditional electrode materials, as it can withstand harsh chemical conditions between pH 2 and 12 after vigorous stirring in 10 mL at room temperature. It slowly dissociates at pH 14 after one week and at pH 1 in one day. Intensive exfoliation of large crystals was observed due to rigorous stirring in a variety of chemical media. Still, no patterns of dissolving in acids and bases were observed, and the crystal structure remained intact. The organic–inorganic hybrid structure of [Cu(2,2′-bpy)VO($O_3PC_6H_5$)$_2$] combines the properties of organic materials and metal oxides on the same platform, where more than 50% of [Cu(2,2′-bpy)VO($O_3PC_6H_5$)$_2$] by mass is composed of polyaromatic moieties. In a pH-neutral environment, the electrochemical behavior differs from that observed under acidic or alkaline conditions. Here, the reversible redox process proceeds more slowly, as indicated by the reduced specific capacitance values. This suggests that diffusional processes play a more dominant role than capacitive mechanisms, indicating that metal-binding phosphonate groups enhance chemical stability, thereby limiting hydrolysis at pH 2 and 12.

Furthermore, [Cu(2,2′-bpy)VO($O_3PC_6H_5$)$_2$] provides a high specific capacitance of 140 F/g in H_3PO_4 at pH 4 and in NaOH at pH 10. The high capacitance at milder and environmentally friendlier electrolytes [Cu(2,2′-bpy)VO($O_3PC_6H_5$)$_2$] is advantageous compared to other materials. For example, materials such as MXene or many carbon-based electrodes require extremely acidic and basic aqueous electrolytes such as 3 M H_2SO_4 or 6 M KOH to reach similar specific capacitance. Furthermore, [Cu(2,2′-bpy)VO($O_3PC_6H_5$)$_2$] can be synthesized sustainably in water at 180°C. [Cu(2,2′-bpy)VO($O_3PC_6H_5$)$_2$] remains stable over a total of 10000 charge and discharge cycles at pH 4 and 10, demonstrating its stability as a supercapacitor electrode material. These high capacitance values near neutral pH are also significant, as they provide more sustainable working conditions under mild pH values compared to aqueous 6 M KOH, where activated carbon electrodes generally operate. Considering conventional MOFs that are composed of water-soluble metal acetate clusters and metal oxides, instability in aqueous medium and electrolytes, these results are significant for further developing the next generation of electrode materials based on hybrid bimetallic Cu/V-phosphonates.

By combining structural flexibility, semi-conductivity, and chemical stability, [Cu(2,2′-bpy)VO($O_3PC_6H_5$)$_2$] represents a novel class of hybrid materials and provides a framework for the design of durable and environmentally benign electrode architectures for future energy storage technologies.

4 | Methods

4.1 | Chemicals

All chemicals were purchased from standard commercial suppliers such as Fisher Scientific, Thermo Fisher, and Merck and were used without further purification. Deionized water (Type I, 18.2 MΩ·cm) for all syntheses and product washing was freshly prepared using an Arium Mini Ultrapure Water System.

4.2 | Synthesis

A mixture of $CuSO_4 \cdot 5H_2O$ (0.124 g, 0.50 mmol), Na_3VO_4 (0.059 g, 0.32 mmol), phenylphosphonic acid (0.448 g, 2.87 mmol), and 2,2'-bipyridine (0.071 g, 0.45 mmol) was added to a 23 mL polytetrafluoroethylene liner. Subsequently, 10 mL of ultrapure water was added to the liner, and the resulting orange suspension was stirred for two minutes before being placed in a stainless-steel container. The mixture was heated at 185°C for 48 h in a preheated oven and then removed using crucible tongs. Raising the reaction temperature from 180°C (the original procedure) to 185°C was crucial, as it suppressed the formation of trace amounts of Cu(2,2′-bpy)SO_4 side product (less than 5 mass%), improving both the yield and purity of the target compound. The crystals can

also be synthesized at up to 230°C hydrothermally with complete phase purity. After cooling to room temperature, the reaction mixture was transferred to a 50 mL centrifuge tube and thoroughly washed with ultrapure water and acetone (approximately 100 mL each, in several aliquots). The resulting product, obtained as green rods or plates, was dried under vacuum at 60°C. The approximate yield was 90% based on vanadium at 185°C.

4.3 | X-Ray Diffraction

X-ray diffractograms were recorded on a Bruker D2 Phaser diffractometer (300 W, 30 kV, 10 mA) using Cu-Kα radiation (λ = 1.5418 Å). Measurements were performed at room temperature over a 2θ range of 2°–50° with a total scan time of 30 min. The data analysis was conducted using the software *Match!* (version 3.3.0, Crystal Impact). Diffractograms of the electrodes used in electrochemical characterization using a D8 Discover diffractometer (Bruker AXS) with a copper X-ray source (Cu-Kα, λ = 1.5406 Å, 40 kV, 40 mA), a Göbel mirror, and a 1 mm point focus. The samples were fixed to a glass sample holder at a desired amount for preparation. Another glass substrate was gently pressed onto the sample to ensure homogeneity, and the excess sample was removed from the glass substrate.

4.4 | Electrode Preparation

The electrodes used in the electrochemical testing were prepared using [Cu(2,2′-bpy)VO($O_3PC_6H_5$)$_2$] as active material and carbon black (ACB, BP2000 from Cabot). For the preparation, 70 mass% of the active material and 20 mass% carbon black were mixed with 10 mass% of binder (polytetrafluoroethylene, 60 mass% dispersion in water, Merck) and ethanol in a mortar. Then, the materials were thoroughly triturated until a homogeneous mixture of dough was formed, and rolled and pressed with a calendaring machine (HR01 hot rolling machine, MTI) and dried at 100°C for 12 h under a vacuum of 6 kPa to form a sheet with a 430 µm thickness, measured using a C640 thickness tester from Labthink. The electrodes with a 10 mm diameter were punched out and characterized. For comparison, electrodes of few-layer $Ti_3C_2T_X$ (Nanoplexus 99%) were prepared following the same methodology.

The electrode morphology was examined using SEM and X-ray diffraction before and after electrochemical testing. SEM was performed using a ZEISS GEMINI 500 microscope with an Xmax detector from Oxford Instruments at an acceleration voltage of 2 kV. Raman analysis was done using a Renishaw InVia microscope with an excitation laser of 532 nm and a power of 87 µW. The spectra were obtained from 10 points with a 10 s exposure time and accumulated five times, then treated for cosmic ray removal and normalization.

Three-electrode polyethylene-ether-ketone (PEEK) cells equipped with spring-loaded graphite pistons were used for electrochemical investigations [63]. The cells were assembled using a glass microfiber membrane (GF/A, Whatman) as a separator sandwiched between two electrodes: the working electrode of active material and the counter-electrode prepared using YP80F. The aqueous electrolytes consisted of phosphoric acid 0.1 mM (Sigma–Aldrich 99%) with pH 4, sodium sulfate 1 M (Sigma–Aldrich 99%) with pH 7, and sodium hydroxide 0.1 mM (Sigma–Aldrich 99%) with pH 10. The electrochemical behavior of the active material was initially investigated using electrochemical impedance spectroscopy, performed from 100 kHz to 10 mHz at an open circuit potential of +0.02 V vs. Ag/AgCl (3 M) for 1 h. All tests were conducted at 25 ± 1°C in a climate chamber using a BioLogic VMP-300 potentiostat/galvanostat. Cyclic voltammetry was performed in different scan rates (1–100 mV/s) in a potential window of −0.8 to +0.8 V vs. Ag/AgCl (3 M). The electrochemical stability and specific capacitance of the active material were investigated using galvanostatic cycling with potential limitation (GCPL, at 1000 mA/g), where the specific capacitance (C_s in F/g) was calculated from each cycle discharge with constant current, following Equation (1):

$$C_s = \frac{i \cdot \Delta t}{m \cdot \Delta E} \quad (1)$$

where i (A) is the applied current, Δt (s) is the discharge time variation, m (g) is the total mass of the electrodes, and ΔE (V) is the potential vs. Ag/AgCl (V) corrected from the Ohmic drop. Furthermore, the stability of the material through the Coulombic efficiency of each cycle is assessed to identify parasitic reactions or degradation of the active material, along with electrolyte decomposition as well.

The morphology of the prepared electrodes was characterized prior to the electrochemical experiments to ensure a thorough characterization of the synthesized material Cu(2,2′-bpy)VO($O_3PC_6H_5$)$_2$. The scanning electron micrographs displayed in Figure S27 indicate a homogenized distribution of the conductive carbon additive over the active material. However, it was possible to observe large smooth-surfaced crystals of the MOF active material, as seen in Figure S28B. At higher magnifications, Figure S28C,D, it is possible to observe layered stacked structures of the material synthesized in acidic conditions, as shown in the scanning micrographs presented in Figure S28, further corroborating the observation of the material stability during electrode preparation.

To further explore the effects of the electrode preparation on the morphology and structure of Cu(2,2′-bpy)VO($O_3PC_6H_5$)$_2$, X-ray diffraction was performed, and the data are displayed in Figure S28E. The diffractogram displays the characteristic reflectance signals of the material at 6.7° 2θ, 13.4° 2θ, and 17.6° 2θ, suggesting no significant changes in the material's structure.

Raman spectroscopy was used to investigate the electrode preparation over the chemical stability of the material, which is presented in Figure S28F. The faint Raman signal at 724 cm^{-1} is associated with a Cu—O stretching vibration of the copper metallic center [64]. The bands around 969 and 998 cm^{-1} are associated with the symmetric stretch of P—O bonds, which also display weaker bands from 405 to 471 cm^{-1} associated with asymmetric stretching and bending of the O—P—O bond deformation [65]. Moreover, it is also possible to observe the bands corresponding to the O—V—O bonds in the range of 338–472 cm^{-1}; symmetric stretching characteristic signals of O—V—O are present at 723 and 771 cm^{-1}, along with a stretching vibration with a frequency

of 855 cm^{-1} [66]. These results further corroborate the presence of two electroactive metallic centers that can undergo redox reactions. At higher frequencies, the C—H and ring deformation of bipyridine molecules are much more prominent, with the characteristic sharp bands displaying at 1147, 1187, 3061, and 3080 cm^{-1} [67, 68].

4.5 | Thermogravimetric Analysis

Thermogravimetric analysis (TGA) measurements were performed under air using a TG Tarsus 209 F3 instrument (Netzsch). A gas flow rate of 10 cm^3/min was applied. Samples were heated from 30°C to 1000°C at a heating rate of 10°C/min.

4.6 | Scanning Electron Microscopy and Energy-Dispersive X-Ray Spectroscopy

Scanning electron micrographs of the samples were acquired using a JEOL JSM-6510 scanning electron microscope. Prior to imaging, the samples were sputter-coated with gold using a JEOL JFC-1200 Fine Coater. The electrode micrographs were collected with a ZEISS GEMINI 500 scanning electron microscope by applying an accelerating voltage of 2 kV at a working distance of 4.0 mm. Before the measurements, the samples were mounted on an aluminum stub, which was fixed with copper tape. Energy-dispersive X-ray spectra and elemental mapping were obtained using a Bruker XFlash Detector 410-M.

4.7 | Raman Spectroscopy

Raman analysis was done using a Renishaw InVia microscope with an excitation laser of 532 nm and a power of 87 μW. The spectra were obtained from 10 points with a 10 s exposure time and accumulated five times, then treated for cosmic ray removal and normalization.

4.8 | pH-Measurements

The pH of ultrapure water was adjusted to values between pH 1 and 14 using aqueous HCl (w = 0.37) and KOH (1 M). For pH = 1 or 14, pure aqueous HCL solution (0.1 M) or KOH solution (1 M) was used directly. All pH measurements were performed at room temperature (20°C) using a Metrohm 744 pH meter.

Author Contributions

T.M. reproduced the compound, optimized the synthesis, calculated the band gap measurements with the help of G.K. and M.S., and performed stability tests. J.G.A.R. performed the electrochemical characterization, Raman spectroscopy, SEM, and XRD characterization of the electrodes and wrote the corresponding section. B.B. wrote the section about the mechanical properties and created the crystal structure pictures and videos. D.S. performed the AFM experiments and calculated the mechanical properties. A.L. performed SEM, and P. T. reproduced the compound for mechanical testing. C.J. contributed to the data visualization. F.E. supervised the mechanical flexibility work. V.P. supervised the supercapacitor and battery work, critically read and revised the manuscript. G.Y. synthesized the first batch of the compound, created the hypothesis, wrote the manuscript introduction, and supervised the work.

Acknowledgements

G.Y. thanks DFG for funding via DFG YU 267/2-1 and DFG YU 267/9-1. M.S. is grateful for funding from the "Young College" of the North-Rhine Westphalian Academy of Sciences, Humanities, and the Arts. J.G.A.R and V.P thank Dr. Oliver Janka from Saarland University for XRD experiments.

Open access funding enabled and organized by Projekt DEAL.

Conflicts of Interest

Gündoğ Yücesan is listed as the inventor of a patent protecting the rights of metal phosphonate electrodes.

Data Availability Statement

The data that support the findings of this study are available in the supplementary material of this article.

References

1. Y. Zhang, E. H. Ang, Y. Yang, M. Ye, W. Du, and C. C. Li, "Interlayer Chemistry of Layered Electrode Materials in Energy Storage Devices," *Advanced Functional Materials* 31 (2021): 2007358, https://doi.org/10.1002/adfm.202007358.

2. L. L. Zhang and X. Zhao, "Carbon-Based Materials As Supercapacitor Electrodes," *Chemical Society Reviews* 38 (2009): 2520–2531, https://doi.org/10.1039/b813846j.

3. Y. He, W. Chen, X. Li, et al., "Freestanding Three-Dimensional Graphene/MnO_2 Composite Networks As Ultralight and Flexible Supercapacitor Electrodes," *ACS Nano* 7 (2013): 174–182, https://doi.org/10.1021/nn304833s.

4. Q. Ke and J. Wang, "Graphene-Based Materials For Supercapacitor Electrodes—A Review," *Journal of Materiomics* 2 (2016): 37–54, https://doi.org/10.1016/j.jmat.2016.01.001.

5. J. Libich, J. Máca, J. Vondrák, O. Čech, and M. Sedlaříková, "Supercapacitors: Properties and Applications," *Journal of Energy Storage* 17 (2018): 224–227, https://doi.org/10.1016/j.est.2018.03.012.

6. Y. Gao, J. Wu, W. Zhang, et al., "Synthesis of Nickel Oxalate/Zeolitic Imidazolate Framework-67 (NiC_2O_4/ZIF-67) as a Supercapacitor Electrode," *New Journal of Chemistry* 39 (2015): 94–97, https://doi.org/10.1039/c4nj01719f.

7. W. Bao, H. Shen, G. Zeng, et al., "Engineering the Next Generation of MXenes: Challenges and Strategies For Scalable Production And Enhanced Performance," *Nanoscale* 17 (2025): 6204–6265, https://doi.org/10.1039/d4nr04560b.

8. H. H. Hegazy, J. Khan, N. Shakeel, et al., "2D-Based Electrode Materials For Supercapacitors—Status, Challenges, And Prospects," *RSC Advances* 14 (2024): 32958–32977, https://doi.org/10.1039/D4RA05473C.

9. S. A. Kadam, K. P. Kadam, and N. R. Pradhan, "Advancements in 2D MXene-Based Supercapacitor Electrodes: Synthesis, Mechanisms, Electronic Structure Engineering, Flexible Wearable Energy Storage For Real-World Applications, And Future Prospects," *Journal of Materials Chemistry A* 12 (2024): 17992–18046, https://doi.org/10.1039/D4TA00328D.

10. B. Chettiannan, E. Dhandapani, G. Arumugam, R. Rajendran, and M. Selvaraj, "Metal-Organic Frameworks: A Comprehensive Review On Common Approaches To Enhance The Energy Storage Capacity In Supercapacitor," *Coordination Chemistry Reviews* 518 (2024): 216048, https://doi.org/10.1016/j.ccr.2024.216048.

11. S. Gautam, S. Rialach, S. Paul, and N. Goyal, "MOF/Graphene Oxide Based Composites In Smart Supercapacitors: A Comprehensive Review On The Electrochemical Evaluation And Material Development For

Advanced Energy Storage Devices," *RSC Advances* 14 (2024): 14311–14339, https://doi.org/10.1039/D4RA01027B.

12. S.-J. Shin, J. W. Gittins, C. J. Balhatchet, A. Walsh, and A. C. Forse, "Metal–Organic Framework Supercapacitors: Challenges and Opportunities," *Advanced Functional Materials* 34 (2024): 2308497, https://doi.org/10.1002/adfm.202308497.

13. A. J. Clancy, H. Au, N. Rubio, G. O. Coulter, and M. S. P. Shaffer, "Understanding and Controlling The Covalent Functionalisation Of Graphene," *Dalton Transactions* 49 (2020): 10308–10318, https://doi.org/10.1039/d0dt01589j.

14. R. A. Murugesan and K. C. Nagamuthu Raja, "Capacitance Performance of $Ti_3C_2T_x$ MXene Nanosheets On Alkaline And Neutral Electrolytes," *Materials Research Bulletin* 163 (2023): 112217, https://doi.org/10.1016/j.materresbull.2023.112217.

15. B. Pal, S. Yang, S. Ramesh, V. Thangadurai, and R. Jose, "Electrolyte Selection For Supercapacitive Devices: A Critical Review," *Nanoscale Advances* 1 (2019): 3807–3835, https://doi.org/10.1039/C9NA00374F.

16. P. Simon and Y. Gogotsi, "Materials for Electrochemical Capacitors," *Nature Materials* 7 (2008): 845–854, https://doi.org/10.1038/nmat2297.

17. H. Xia, Y. S. Meng, G. Yuan, C. Cui, and L. Lu, "A Symmetric RuO_2/RuO_2 Supercapacitor Operating at 1.6 V by Using a Neutral Aqueous Electrolyte," *Electrochemical and Solid-State Letters* 15 (2012): A60, https://doi.org/10.1149/2.023204esl.

18. M. Naguib, M. Kurtoglu, V. Presser, et al., "Two-Dimensional Nanocrystals Produced by Exfoliation of Ti_3AlC_2," *Advanced Materials* 23 (2011): 4248–4253, https://doi.org/10.1002/adma.201102306.

19. B. Anasori, M. R. Lukatskaya, and Y. Gogotsi, "2D Metal Carbides And Nitrides (MXenes) for Energy Storage," *Nature Reviews Materials* 2 (2017): 16098, https://doi.org/10.1038/natrevmats.2016.98.

20. J. Luo, W. Zhang, H. Yuan, et al., "Pillared Structure Design of MXene With Ultralarge Interlayer Spacing for High-Performance Lithium-Ion Capacitors," *ACS Nano* 11 (2017): 2459–2469, https://doi.org/10.1021/acsnano.6b07668.

21. D. Xiong, X. Li, Z. Bai, and S. Lu, "Recent Advances in Layered $Ti_3C_2T_x$ MXene for Electrochemical Energy Storage," *Small* 14 (2018): 1703419, https://doi.org/10.1002/smll.201703419.

22. J. Xiao, X. Cao, B. Gridley, et al., "From Mining to Manufacturing: Scientific Challenges and Opportunities Behind Battery Production," *Chemical Reviews* 125 (2025): 6397–6431, https://doi.org/10.1021/acs.chemrev.4c00980.

23. R. Marom, S. F. Amalraj, N. Leifer, D. Jacob, and D. Aurbach, "A Review Of Advanced And Practical Lithium Battery Materials," *Journal of Materials Chemistry* 21 (2011): 9938–9954, https://doi.org/10.1039/C0JM04225K.

24. S.-K. Su, C.-P. Chuu, M.-Y. Li, C.-C. Cheng, H.-S. P. Wong, and L.-J. Li, "Layered Semiconducting 2D Materials for Future Transistor Applications," *Small Structures* 2 (2021): 2000103, https://doi.org/10.1002/sstr.202000103.

25. G. Wang, L. Zhang, and J. Zhang, "A Review of Electrode Materials for Electrochemical Supercapacitors," *Chemical Society Reviews* 41 (2012): 797–828, https://doi.org/10.1039/c1cs15060j.

26. H. Furukawa, K. E. Cordova, M. O'Keeffe, and O. M. Yaghi, "The Chemistry and Applications of Metal-Organic Frameworks," *Science* 341 (2013): 1230444, https://doi.org/10.1126/science.1230444.

27. D. Sheberla, "Conductive MOF Electrodes for Stable Supercapacitors With High Areal Capacitance," *Nature Materials* 16 (2017): 220–224, https://doi.org/10.1038/nmat4766.

28. M. O'Keeffe, "Design of MOFs and Intellectual Content in Reticular Chemistry: A Personal View," *Chemical Society Reviews* 38 (2009): 1215–1217, https://doi.org/10.1039/b802802h.

29. C. A. Peeples, D. Kober, F.-J. Schmitt, et al., "A 3D Cu-Naphthalene-Phosphonate Metal–Organic Framework With Ultra-High Electrical Conductivity," *Advanced Functional Materials* 31 (2021): 2007294, https://doi.org/10.1002/adfm.202007294.

30. G. Yücesan, Y. Zorlu, M. Stricker, and J. Beckmann, "Metal-Organic Solids Derived From Arylphosphonic Acids," *Coordination Chemistry Reviews* 369 (2018): 105–122, https://doi.org/10.1016/j.ccr.2018.05.002.

31. P. Tholen, L. Wagner, J. G. A. Ruthes, et al., "A New Family of Layered Metal-Organic Semiconductors: Cu/V-Organophosphonates," *Small* 19 (2023): 2304057, https://doi.org/10.1002/smll.202304057.

32. K. Siemensmeyer, C. A. Peeples, P. Tholen, et al., "Phosphonate Metal–Organic Frameworks: A Novel Family of Semiconductors," *Advanced Materials* 32 (2020): 2000474, https://doi.org/10.1002/adma.202000474.

33. C. Ribeiro, B. Tan, F. Figueira, et al., "Mixed Ionic and Electronic Conductivity in a Tetrathiafulvalene-Phosphonate Metal–Organic Framework," *Journal of the American Chemical Society* 147 (2025): 63–68, https://doi.org/10.1021/jacs.4c13792.

34. G. Yucesan, V. Golub, C. J. O'Connor, and J. Zubieta, "Solid State Coordination Chemistry Of The Copper(II)-Terpyridine/Oxovanadium Organophosphonate System: Hydrothermal Syntheses, Structural Characterization And Magnetic Properties," *Dalton Transactions* (2005): 2241–2251, https://doi.org/10.1039/b502073e.

35. G. Yucesan, V. Golub, C. J. O'Connor, and J. Zubieta, "Temperature Dependence Of The Crystal Chemistry Of The Oxovanadium–Ethylenediphosphonate/Copper(II)–Bipyridine System. Crystal Structures Of The Two-Dimensional $[Cu(bpy)VO_2(O_3PCH_2CH_2PO_3H)]\cdot 1.5H_2O$ and of the One-Dimensional $[Cu(bpy)VO_2(O_3PCH_2CH_2PO_3H)]$," *Solid State Sciences* 7 (2005): 133–139, https://doi.org/10.1016/j.solidstatesciences.2004.10.010.

36. G. Yucesan, M. H. Yu, W. Ouellette, C. J. O'Connor, and J. Zubieta, "Secondary Metal–Ligand Cationic Subunits {ML}n+ As Structural Determinants In The Oxovanadium/Phenylphosphonate/{ML}n+ System, Where {ML} is a Cu^{2+}/Organonitrogen Moiety," *CrystEngComm* 7 (2005): 480–490, https://doi.org/10.1039/B506250K.

37. P. Hu, P. Hu, T. D. Vu, et al., "Vanadium Oxide: Phase Diagrams, Structures, Synthesis, and Applications," *Chemical Reviews* 123 (2023): 4353–4415, https://doi.org/10.1021/acs.chemrev.2c00546.

38. A. Clearfield and K. Demadis, *Metal Phosphonate Chemistry: From Synthesis to Applications* (Royal Society of Chemistry Publishing, 2012).

39. B. Bhattacharya, A. A. L. Michalchuk, D. Silbernagl, et al., "A Mechanistic Perspective on Plastically Flexible Coordination Polymers," *Angewandte Chemie International Edition* 59 (2020): 5557–5561, https://doi.org/10.1002/anie.201914798.

40. B. Bhattacharya, A. A. L. Michalchuk, D. Silbernagl, et al., "An Atomistic Mechanism For Elasto-Plastic Bending In Molecular Crystals," *Chemical Science* 14 (2023): 3441–3450, https://doi.org/10.1039/d2sc06470g.

41. X. Liu, A. A. L. Michalchuk, B. Bhattacharya, N. Yasuda, F. Emmerling, and C. R. Pulham, "High-Pressure Reversibility In A Plastically Flexible Coordination Polymer Crystal," *Nature Communications* 12 (2021): 3871, https://doi.org/10.1038/s41467-021-24165-x.

42. G. Yucesan, W. Ouellette, V. Golub, C. J. O'Connor, and J. Zubieta, "Solid State Coordination Chemistry: Temperature Dependence Of The Crystal Chemistry of the Oxovanadium-phenylphosphonate-copper(II)-2,2′-bipyridine system. Crystal Structures of the One-Dimensional $[\{Cu(bpy)\}VO_2(O_3PC_6H_5)(HO_3PC_6H_5)]$, $[\{Cu_3(bpy)_3(H_2O)\}V_4O_9(O_3PC_6H_5)_4]$, $[\{Cu(bpy)\}_2V_3O_6(O_3PC_6H_5)_3(HO_3PC_6H_5)]$ and $[\{Cu(bpy)\}VO(O_3PC_6H_5)_2]$," *Solid State Sciences* 7 (2005): 445–458, https://doi.org/10.1016/j.solidstatesciences.2005.01.009.

43. G. R. Krishna, R. Devarapalli, G. Lal, and C. M. Reddy, "Mechanically Flexible Organic Crystals Achieved by Introducing Weak Interactions in Structure: Supramolecular Shape Synthons," *Journal of the American Chemical Society* 138 (2016): 13561–13567, https://doi.org/10.1021/jacs.6b05118.

44. C. M. Reddy, R. C. Gundakaram, S. Basavoju, M. T. Kirchner, K. A. Padmanabhan, and G. R. Desiraju, "Structural Basis For Bending Of Organic Crystals," *Chemical Communications* (2005): 3945–3947, https://doi.org/10.1039/b505103g.

45. M. Dakovic, M. Borovina, M. Pisacic, et al., "Mechanically Responsive Crystalline Coordination Polymers With Controllable Elasticity," *Angewandte Chemie International Edition* 57 (2018): 14801–14805, https://doi.org/10.1002/anie.201808687.

46. S. Kusumoto, A. Sugimoto, Y. Zhang, Y. Kim, M. Nakamura, and S. Hayami, "Elastic Crystalline Fibers Composed of a Nickel(II) Complex," *Inorganic Chemistry* 60 (2021): 1294–1298, https://doi.org/10.1021/acs.inorgchem.0c03295.

47. J. Tauc, "Optical Properties and Electronic Structure of Amorphous Ge and Si," *Materials Research Bulletin* 3 (1968): 37–46, https://doi.org/10.1016/0025-5408(68)90023-8.

48. J. Tauc, R. Grigorovici, and A. Vancu, "Optical Properties and Electronic Structure of Amorphous Germanium," *Physica Status Solidi (b)* 15 (1966): 627–637, https://doi.org/10.1002/pssb.19660150224.

49. L. Mai, H. Li, Y. Zhao, et al., "Fast Ionic Diffusion-Enabled Nanoflake Electrode by Spontaneous Electrochemical Pre-Intercalation for High-Performance Supercapacitor," *Scientific Reports* 3 (2013): 1718, https://doi.org/10.1038/srep01718.

50. C. Liu, X. Chi, Q. Han, and Y. Liu, "Acid-Alkaline Electrolytes: A High Energy Density Aqueous Battery Achieved by Dual Dissolution/Deposition Reactions Separated in Acid-Alkaline Electrolyte (Adv. Energy Mater. 12/2020)," *Advanced Energy Materials* 10 (2020): 2070053, https://doi.org/10.1002/aenm.202070053.

51. M. R. Lukatskaya, S. Kota, Z. Lin, et al., "Ultra-High-Rate Pseudocapacitive Energy Storage In Two-Dimensional Transition Metal Carbides," *Nature Energy* 2 (2017): 17105, https://doi.org/10.1038/nenergy.2017.105.

52. C. Zhong, Y. Deng, W. Hu, J. Qiao, L. Zhang, and J. Zhang, "A Review Of Electrolyte Materials And Compositions For Electrochemical Supercapacitors," *Chemical Society Reviews* 44 (2015): 7484–7539, https://doi.org/10.1039/C5CS00303B.

53. S. Ardizzone, G. Fregonara, and S. Trasatti, ""Inner" And "Outer" Active Surface of RuO_2 Electrodes," *Electrochimica Acta* 35 (1990): 263–267, https://doi.org/10.1016/0013-4686(90)85068-X.

54. T. Brezesinski, J. Wang, S. H. Tolbert, and B. Dunn, "Ordered Mesoporous α-MoO_3 With Iso-Oriented Nanocrystalline Walls for Thin-Film Pseudocapacitors," *Nature Materials* 9 (2010): 146–151, https://doi.org/10.1038/nmat2612.

55. M. Zhao, S. Kariuki, H. D. Dewald, et al., "Electrochemical Stability of Copper in Lithium-Ion Battery Electrolytes," *Journal of The Electrochemical Society* 147 (2000): 2874, https://doi.org/10.1149/1.1393619.

56. H. Su, Y. Song, Y. Hu, et al., "A Copper-Based Polycarbonyl Coordination Polymer as a Cathode for Li Ion Batteries," *Crystal Growth & Design* 21 (2021): 3668–3676, https://doi.org/10.1021/acs.cgd.0c01578.

57. Y. Luo, J. Liu, and L. A. Zhang, "A Monocrystalline Coordination Polymer With Multiple Redox Centers as a High-Performance Cathode for Lithium-Ion Batteries," *Angewandte Chemie International Edition* 61 (2022): 202209458, https://doi.org/10.1002/anie.202209458.

58. J. Liu, M. Zheng, S. Wu, and L. Zhang, "Design Strategies For Coordination Polymers As Electrodes And Electrolytes In Rechargeable Lithium Batteries," *Coordination Chemistry Reviews* 483 (2023): 215084, https://doi.org/10.1016/j.ccr.2023.215084.

59. Y. Cao, Y. He, H. Gang, et al., "Stability Study Of Transition Metal Oxide Electrode Materials," *Journal of Power Sources* 560 (2023): 232710, https://doi.org/10.1016/j.jpowsour.2023.232710.

60. K. D. Demadis, S. D. Katarachia, and M. Koutmos, "Crystal Growth And Characterization Of Zinc–(amino-tris-(methylenephosphonate)) Organic–Inorganic Hybrid Networks And Their Inhibiting Effect On Metallic Corrosion," *Inorganic Chemistry Communications* 8 (2005): 254–258, https://doi.org/10.1016/j.inoche.2004.12.019.

61. R. J. Motekaitis, I. Murase & A. E. Martell, and N. Equilibriums of ethylenediamine-N,, "Equilibriums of ethylenediamine-N,N,N',N'-tetrakis(methylenephosphonic) acid With copper(II), nickel(II), cobalt(II), zinc(II), magnesium(II), calcium(II), and iron(III) Ions In Aqueous Solution," *Inorganic Chemistry* 15 (1976): 2303–2306, https://doi.org/10.1021/ic50163a066.

62. D. R. Lide, *CRC Handbook of Chemistry and Physics* (CRC Press, 2004).

63. D. Weingarth, M. Zeiger, N. Jäckel, M. Aslan, G. Feng, and V. Presser, "Graphitization as a Universal Tool to Tailor the Potential-Dependent Capacitance of Carbon Supercapacitors," *Advanced Energy Materials* 4 (2014): 1400316, https://doi.org/10.1002/aenm.201400316.

64. I. E. Valenzuela, J. C. Muñoz-Acevedo, E. Pabón, and A. P. S. Paim, "Cu (II)-Based Metal-Organic Framework Functionalized With Graphene Oxide As A Sorbent For The Dispersive Micro-Solid-Phase Extraction Of Losartan Potassium From Water," *Journal of Porous Materials* 31 (2024): 1737–1752, https://doi.org/10.1007/s10934-024-01620-w.

65. Z. Z. Zhang, F. Zhang, G. Q. Li, J. Zhang, and W. F. Zhang, "Red-Emitting Phosphor Series: $Ca_9Y(PO_4)_7(1\text{-}x)(VO_4)7_x{:}Eu^{3+}$ (x = 0 − 1) With Improved Luminescence Thermal Stability By Anionic Polyhedron Substitution," *Journal of Materials Science: Materials in Electronics* 30 (2019): 8838–8846, https://doi.org/10.1007/s10854-019-01210-6.

66. J. L. Blin, A. Lorriaux-Rubbens, F. Wallart, and J. P. Wignacourt, "Synthesis and Structural Investigation of the Eu_{1-x} Bi_xVO_4 Scheelite Phase: X-Ray Diffraction, Raman Scattering And Eu^{3+} Luminescence," *Journal of Materials Chemistry* 6 (1996): 385–389, https://doi.org/10.1039/jm9960600385.

67. E. Castellucci, L. Angeloni, N. Neto, and G. Sbrana, "IR and Raman Spectra of A 2,2′-bipyridine Single Crystal: Internal Modes," *Chemical Physics* 43 (1979): 365–373, https://doi.org/10.1016/0301-0104(79)85204-0.

68. C. Lapouge, G. Buntinx, and O. Poizat, "Resonance Raman Spectra Simulation of the 4,4′-Bipyridine Anion Radical and N-Protonated Radical," *The Journal of Physical Chemistry A* 106 (2002): 4168–4175, https://doi.org/10.1021/jp013869s.

Supporting Information

Additional supporting information can be found online in the Supporting Information section.

Supporting File 1: adfm74279-sup-0001-SuppMat.pdf.

Supporting File 2: adfm74279-sup-0002-VideoS1–S4.zip.